Magn Reson Mater Phy (2012) 25:419–431
DOI 10.1007/s10334-012-0314-y

RESEARCH ARTICLE

Practical considerations for in vivo MRI with higher dimensional spatial encoding

Daniel Gallichan · Chris A. Cocosco · Gerrit Schultz · Hans Weber · Anna M. Welz · Jürgen Hennig · Maxim Zaitsev

Received: 21 December 2011 / Revised: 6 March 2012 / Accepted: 14 March 2012 / Published online: 7 April 2012

Abstract
Object This work seeks to examine practical aspects of in vivo imaging when spatial encoding is performed with three or more encoding channels for a 2D image.
Materials and methods The recently developed 4-Dimensional Radial In/Out (4D-RIO) trajectory is compared in simulations to an alternative higher-order encoding scheme referred to as O-space imaging. Direct comparison of local *k*-space representations leads to the proposal of a modification to the O-space imaging trajectory based on a scheme of prephasing to improve the reconstructed image quality. Data were collected using a 4D-RIO acquisition in vivo in the human brain and several image reconstructions were compared, exploiting the property that the dense encoding matrix, after a 1D or 2D Fourier transform, can be approximated by a sparse matrix by discarding entries below a chosen magnitude.
Results The proposed prephasing scheme for the O-space trajectory shows a marked improvement in quality in the simulated image reconstruction. In experiments, 4D-RIO data acquired in vivo in the human brain can be reconstructed to a reasonable quality using only 5 % of the encoding matrix—massively reducing computer memory requirements for a practical reconstruction.
Conclusion Trajectory design and reconstruction techniques such as these may prove especially useful when extending generalized higher-order encoding methods to 3D images.

Keywords MRI · Nonlinear spatial encoding · Non-Fourier encoding · PatLoc

D. Gallichan · C. A. Cocosco · G. Schultz · H. Weber · A. M. Welz · J. Hennig · M. Zaitsev
University Medical Center Freiburg, Freiburg, Germany

D. Gallichan (✉)
CIBM, EPFL—SB IPSB LIFMET, Section 6, 1015 Lausanne, Switzerland
e-mail: daniel.gallichan@epfl.ch

Introduction

We recently demonstrated the successful reconstruction of images from data collected on a phantom where the spatial encoding was achieved by manipulation of quadrupolar spatial encoding magnetic fields (SEMs) simultaneously with manipulation of conventional linear SEMs [1]. The motivation for these investigations is to extend the concept introduced by PatLoc (**Pa**rallel Imaging **T**echnique using **Loc**alized Gradients) [2], which relaxes the requirement that the SEMs must vary linearly across the field-of-view (FoV). Ambiguities in spatial localization which may arise from encoding with nonlinear SEMs can still be resolved by making use of parallel RF receive arrays and adapted parallel imaging techniques [3]. Increasing the degrees of freedom available for spatial encoding may lead to improved gradient performance or reduced peripheral nerve stimulation (PNS).

When performing spatial encoding with more SEMs than spatial dimensions of the reconstructed image, the choice of an encoding trajectory becomes complicated due to the additional degrees of freedom available. In this work we compare, theoretically and through simulations, encoding using derivatives of two higher-dimensional encoding techniques: the O-space method [4] and a trajectory referred to as 4-Dimensional Radial In/Out (4D-RIO) [1]. Each of these techniques has been shown capable of exploiting the position-dependent spatial resolution of

nonlinear encoding while avoiding the creation of a region towards the center of the FoV where there is no spatial encoding (as results from encoding using only two quadrupolar fields). The O-space method uses two linear encoding fields, x and y, in combination with a bowl-shaped quadratic field, $x^2 + y^2$, to encode a 2D image. The 4D-RIO trajectory encodes with linear x and y in combination with two quadrupolar quadratic fields of the form $x^2 - y^2$ and $2xy$, resulting in four encoding channels for a 2D image. Here we compare these two methods using the concept of local k-space and consider modifications to the O-space method to improve image quality, which we then verify with simulations. The hardware setup we currently have available can generate the quadrupolar fields necessary for 4D-RIO imaging, but does not produce an $x^2 + y^2$ encoding field, so we were unable to perform O-space imaging. All experiments presented here were performed using the 4D-RIO trajectory.

Development of the 4D-RIO trajectory to generate high-quality images from human data presents some particular challenges. Potentially the greatest barrier to high-resolution imaging is the long reconstruction time resulting from the iterative inversion of a very large encoding matrix, which becomes necessary as the speedup offered by the Fast Fourier Transform can no longer be exploited to directly reconstruct the data.

In this work we explore some of the properties of the data acquired using the 4D-RIO trajectory, examining how the encoding matrix might be sparsified, leading to faster reconstructions with lower memory requirements. We also describe some of the extra measures necessary to ensure that use of the sequence is safe for human subjects and present high-resolution 4D-RIO images collected in a healthy volunteer.

Theory

The signal s from RF receive channel α for generalized encoding, neglecting relaxation effects, can be written [3]:

$$s_\alpha(\mathbf{k}) = \int_V m(\mathbf{x}) c_\alpha(\mathbf{x}) e^{-i\mathbf{k}^T \boldsymbol{\psi}(\mathbf{x})} \mathrm{d}\mathbf{x}, \quad (1)$$

where $m(\mathbf{x})$ is the magnetization at position $\mathbf{x}$, $c_\alpha(\mathbf{x})$ is the sensitivity of coil α at position $\mathbf{x}$, and $\boldsymbol{\psi}(\mathbf{x})$ is a multi-dimensional function representing all SEMs, linear and/or nonlinear. $\mathbf{k}$ is a vector of the same length as the number of SEMs, describing the net moment of each SEM. For O-space encoding there are three SEMs, so:

$$\boldsymbol{\psi}(\mathbf{x}) = \{\psi_x(\mathbf{x}); \psi_y(\mathbf{x}); \psi_c(\mathbf{x})\} = \{x; y; x^2 + y^2\}. \quad (2)$$

The 4D-RIO trajectory makes use of 4 SEMs, where:

$$\begin{aligned} \boldsymbol{\psi}(\mathbf{x}) &= \{\psi_x(\mathbf{x}); \psi_y(\mathbf{x}); \psi_a(\mathbf{x}); \psi_b(\mathbf{x})\} \\ &= \{x; y; x^2 - y^2; 2xy\}. \end{aligned} \quad (3)$$

The 4D-RIO trajectory itself consists of simultaneous radial projection trajectories on the linear and quadrupolar SEMs, but with their progressions exactly out of phase with each other, such that when the linear encoding is strongest there is no quadrupolar component present, and vice versa. Our current implementation of this trajectory splits the readout into two sections to allow for the discontinuity during the sweep-back of the linear encoding. During each individual readout event the encoding fields are constant, meaning that the encoding effectively results in a series of projections onto quadratic fields with different positions for the center of the saddle—similar to the trajectory used in O-space acquisitions where linear SEMs were combined with encoding from a bowl-shaped quadratic field [4].

Comparing 4D-RIO and O-space imaging

The trajectory design method previously described for O-space imaging is to select a series of 'center-placements' (CPs) and, by combination of the linear and quadratic fields (as well as a B_0 offset), create a set of effective quadratic encoding fields which are centered on each of the CPs. The CP scheme which was chosen in Stockmann et al. [4] was a set of two concentric circles, plus the center of the FoV as shown in Fig. 1a, but a variety of other CPs are possible [5]. By contrast, 4D-RIO was developed by searching for a simple combination of two 2D trajectories (one for linear (x, y) and one for quadratic (a, b)) which result in a favorable local k-space distribution. Following (1), we define the local k-space vector field, $\mathbf{k}_{\mathrm{loc}}(\mathbf{x}, t)$, as:

$$\mathbf{k}_{\mathrm{loc}}(\mathbf{x}, t) = \nabla\Phi(\mathbf{x}, t). \quad (4)$$

When encoding is applied by purely linear gradients, $\mathbf{k}_{\mathrm{loc}}(\mathbf{x}, t)$ is independent of $\mathbf{x}$, so the local k-space collapses to being equal to the 'traditional' k-space throughout the FoV. For more general trajectories, a grid of points may be chosen across the nominal field of view and a separate local k-space plot calculated for each location. Figure 2d shows the local k-space over a 7×7 grid for the 4D-RIO trajectory, and it can be compared with the local k-space for the concentric ring CP O-space (which we refer to here as CRCPO to remain specific when referring to a trajectory) in Fig. 2a. Both local k-space distributions suggest that image resolution is expected to be lower towards the center of the FoV (as the extent of the local k-space coverage is reduced towards the center) and higher at the FoV perimeter. This figure also reveals that the CRCPO has an asymmetric local k-space, with the asymmetry increasing with distance from the FoV center. As a consequence, we would expect the local resolution

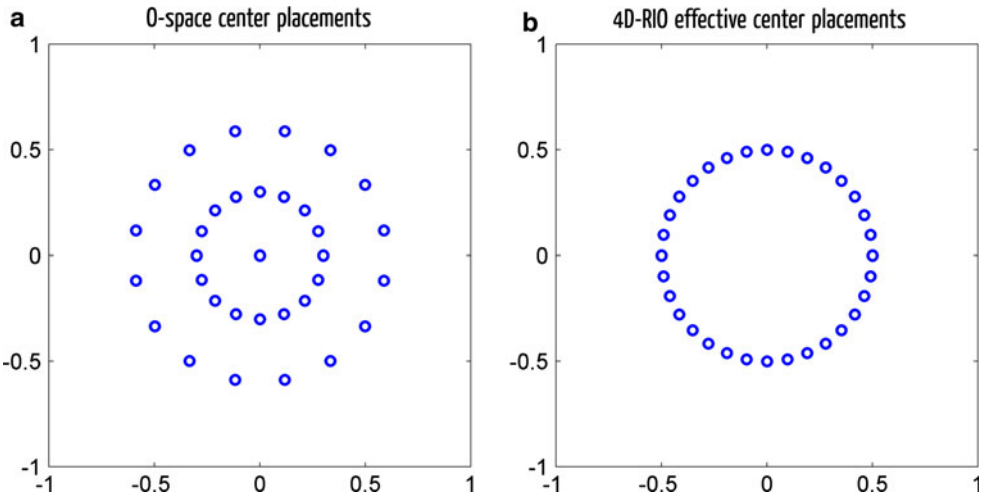

Fig. 1 **a** The chosen center placements (CPs) for an example O-space trajectory (CRCPO) compared with **b** the effective center placements when using the 4D-RIO encoding trajectory, where the FoV runs from −1 to 1 in x and y. The CPs are unaffected by prephasing

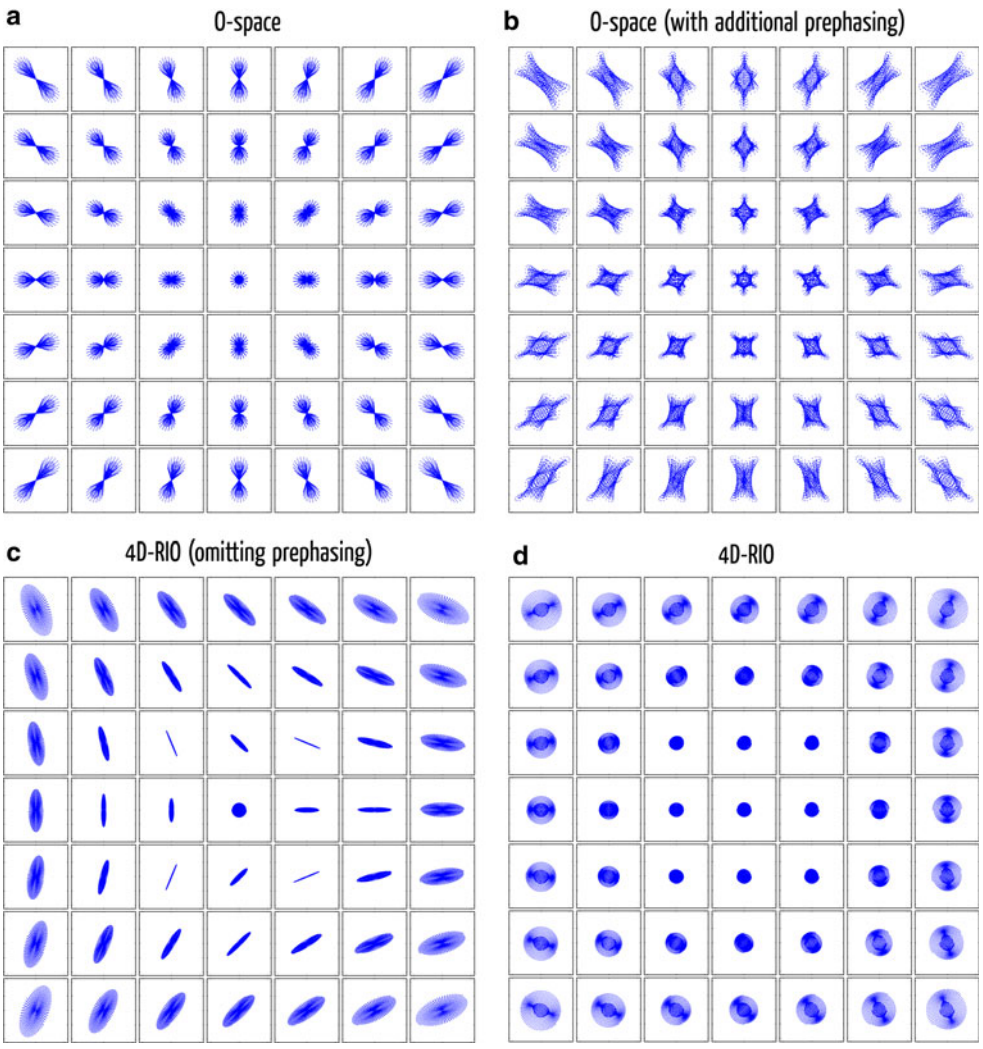

Fig. 2 7 × 7 grids showing the local k-space for **a** an O-space trajectory (CRCPO), and **b** the same trajectory but with sinusoidally varying linear x and y components as prephasing. **c** Local k-space grids for the 4D-RIO trajectory with the prephasing removed and **d** the original 4D-RIO trajectory. Trajectories shown are for 32 × 32 samples for easier visualization (32 × 33 for O-space trajectories to allow for additional central CP)

achievable in the reconstructed image to be reduced in the azimuthal direction (i.e. the direction of poorer local k-space coverage). However, in keeping with the original motivation for O-space imaging, this lack of encoding in the azimuthal direction may be partially compensated by the additional spatial encoding provided by an RF receive array—the contribution of which is not considered in the local k-space plots.

For 4D-RIO we can also calculate the effective CPs for each of the projections acquired; as shown in Fig. 1b, they also form a circle. It should be noted that here we use the definition of CP to refer to the saddle center of the field present during the readout—a single position for each readout event—whereas the saddle center of the net phase distribution can change during the readout, as was shown in [1]. Unlike the CRCPO, however, each projection is defined not only by the CP, but also by the additional phase distribution present even in the middle of the projection (for CRCPO there is no net phase distribution when the center of each projection is reached). This additional phase distribution has some analogies with traditional phase encoding—the readout gradient is identical for the acquisition of each line in *k*-space, but the additional phase provided by the phase-encoding gradient is what remains at the center of each projection. There are also analogies, however, to quadratic phase preparation pulses which have been used to deliberately elicit spatially varying shifts in the local *k*-space [6]. If the additional phase is the same for all readouts, it will simply shift the local *k*-spaces. If the additional phase varies between readouts, however, then it can have a more dramatic effect on the encoding.

To demonstrate the significant effect of the phase present before the readout begins (which we refer to here as 'prephasing') on the local *k*-space, we also calculated local *k*-space plots for the 4D-RIO trajectory as if there were no prephasing present, as shown in Fig. 2c. The CPs for this trajectory are the same as for the standard 4D-RIO, but removal of the prephasing leads to very different local *k*-spaces, with many regions of the image expected to have strongly asymmetric spatial resolution as a result. Having identified the prephasing as the major difference between the trajectories for 4D-RIO and CRCPO, we can also consider what happens if we choose to add prephasing to the CRCPO trajectory—exploiting the additional degrees of freedom this introduces in order to create more desirable local *k*-space distributions. Obviously there remains a large choice of potential patterns which could be chosen as the prephasing, but here we chose to use a similar form to that resulting from 4D-RIO: linear *x* and *y* components which vary sinusoidally moving around the circles of the CPs. A simple trajectory which maintains favorable symmetry in local *k*-space across the entire FoV was found by concatenating two copies of the CRCPO trajectory with half the number of samples per readout—thus creating the same number of 'spokes' as for 4D-RIO (apart from the additional central CP for CRCPO). The prephasing with constant amplitude equivalent to FoV/2 in (k_x, k_y)-space was then applied with a sinusoidal variation of the linear *x* and *y* gradients to achieve a full cycle across both repeats of the CPs. The prephasing thus effectively revolves at half the frequency of the rotation of the CPs.

The local *k*-space for the resulting trajectory, CRCPO with prephasing, is shown in Fig. 2b. It can be seen that regions towards the edge of the FoV would be expected to have a more symmetric spatial resolution when compared to the standard CRCPO trajectory. We expect comparisons of this kind to be helpful when designing further higher dimensional trajectories, especially as the shapes of the encoding fields become more complex, such as in [7].

Different levels of prephasing have no influence on the CPs, as the field present during the readout remains the same. The effective *k*-space trajectory in 3 or 4 dimensions, however, will be different. Figure 3a shows the CRCPO trajectory represented in 3 dimensions (k_x, k_y, k_c), and the same trajectory, but with prephasing, is shown in Fig. 3b. The vector direction of each readout line is unaffected by the prephasing—but their positions in the 3D space can be very different. Visualizing the 4D-RIO trajectory in a similar way is complicated by the need to represent four encoding directions in 3D space. Figure 4d shows the 4D-RIO trajectory with (k_x, k_y, k_a) shown in blue, and (k_x, k_y, k_b) in green. Although this representation does not allow full insight into the 4D trajectory, the difference when prephasing is omitted (Fig. 3c) is clearly identifiable.

Image reconstruction

To date, all 4D-RIO data have been reconstructed using a conjugate gradient (CG) method to iterate towards the pseudo-inverse of **E**, the encoding matrix (as previously described in [1] and similar to the method from [8]), which appears in the matrix form of the signal equation (neglecting relaxation):

$$\mathbf{s} = \mathbf{E}\mathbf{m}, \tag{5}$$

where **s** is the column vector of measured signals and **m** is the column vector of magnetization values representing the image of the object. **E** has the dimensions $N_c N_k \times N_\rho$, where N_c is the number of RF coils, N_k is the number of data points acquired and N_ρ is the number of points onto which the image is to be reconstructed. Encoding due to an arbitrary number of SEMs can be included in **E**, as well as the sensitivity profiles of the RF receive coils and the local changes in resonance frequency due to B_0 inhomogeneities. The size of matrix **E** grows rapidly with the number of samples or the reconstruction size, and quickly becomes too large to store in the memory of a typical desktop PC. For example, the images presented in [1] were 128 × 128 samples, 8 RF coils, reconstructed to a 160 × 160 grid. This requires 26.8 GB to store the corresponding **E** as complex values at single precision. This was previously dealt with by calculating the matrix–vector multiplication line-by-line as it is required for each iteration of the reconstruction—making the memory requirements

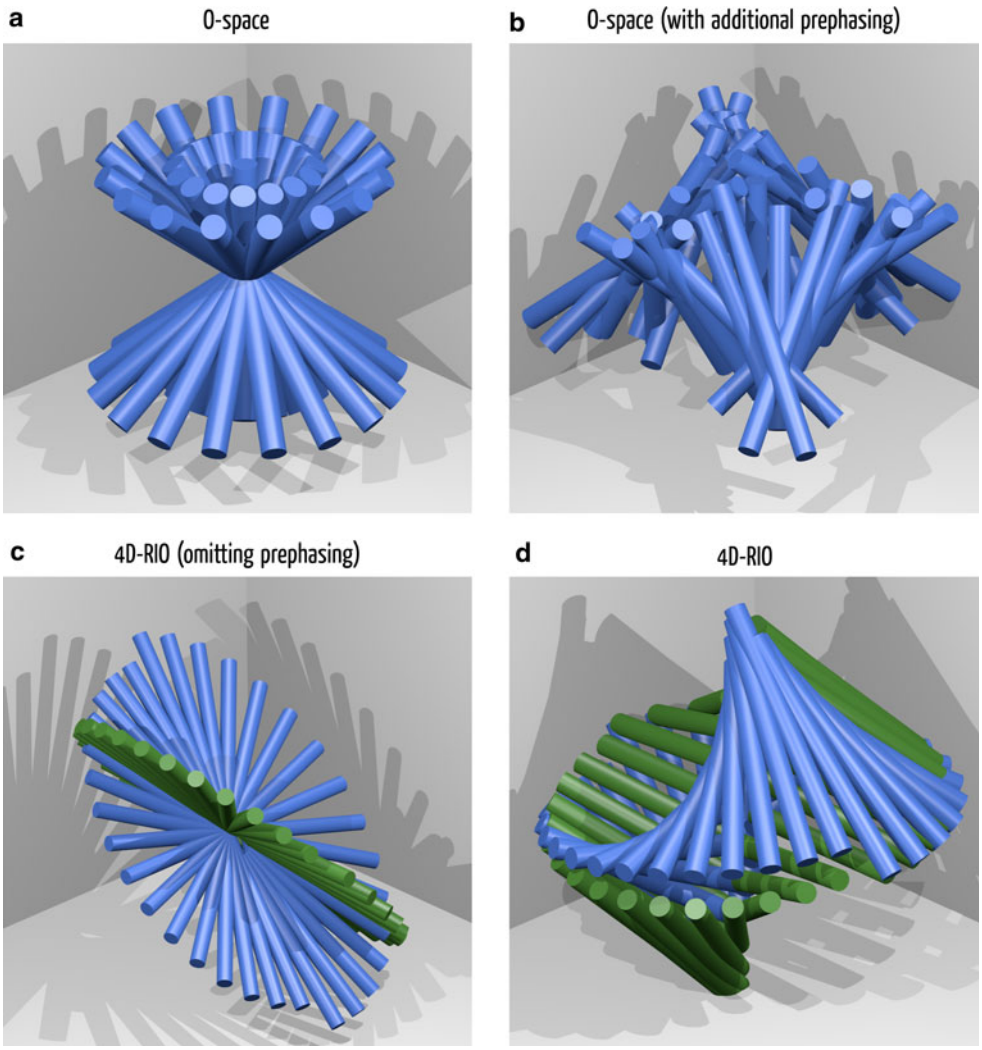

Fig. 3 3D representations (k_x, k_y, k_c) of the effective k-space trajectory followed in O-space **a** before and **b** after the addition of sinusoidally varying prephasing, where each cylinder represents the path of a single readout line. Similar plots for **c** 4D-RIO with prephasing removed and **d** retaining the prephasing. As 4D-RIO encodes with 4 dimensions there are two cylinders for each readout line, one plotted in *blue* as (k_x, k_y, k_a) and the other in *green* as (k_x, k_y, k_b). The projection of each of these plots onto the (k_x, k_y)-plane corresponds exactly to each of the central local k-space plots in Fig. 2. For all plots k_X is the net moment of the SEM ψ_x

negligible, but leading to prohibitively long reconstruction times (at least several hours). Recently large quantities of random access memory (RAM) ($\sim$1–2 TB) have become available for compute servers in a sub-supercomputer price-range, meaning that even reconstructions at twice the resolution mentioned previously and therefore requiring 16 times as much memory (256 $\times$ 256 samples, eight RF coils, reconstructed to 320 $\times$ 320 grid leading to **E** of 420 GB) can be performed with explicit storage of the entire matrix. It has been noted for reconstruction of CRCPO data [4] and 4D-RIO data (in abstract form, [9]) that taking a 1D FFT of both the data and the encoding matrix along the readout direction can lead to a sparse representation of **E**, thereby allowing a fast reconstruction to be performed with much reduced memory requirements—but at the expense of loss of quality in the reconstruction. In this work we explicitly perform the reconstruction with different proportions of the encoding matrix retained, investigating the nature of the artifacts arising from the approximate reconstruction. We can thereby test whether such fast reconstructions are useful when memory requirements are reduced to a level which can be run on a desktop PC with more modest quantities of RAM available.

Methods to reduce RAM requirements of image reconstruction

There are a number of approaches which can be employed to reduce the RAM requirements of the reconstruction without taking the extreme approach of re-calculating each line of the encoding matrix as it is required during each iteration of the reconstruction. A simple approach which reduces the memory requirements by a factor N_c without affecting the quality of the reconstruction is to separate the full matrix **E** into sub-matrices for each RF-coil, as depicted in Fig. 4. The sub-matrix $\mathbf{E}_\phi$, which contains the phase information from the SEM encoding (as well as optionally including off-resonance effects), is repeated N_c times, with each repeat weighted by the individual RF coil sensitivities. This immediately reduces the RAM storage

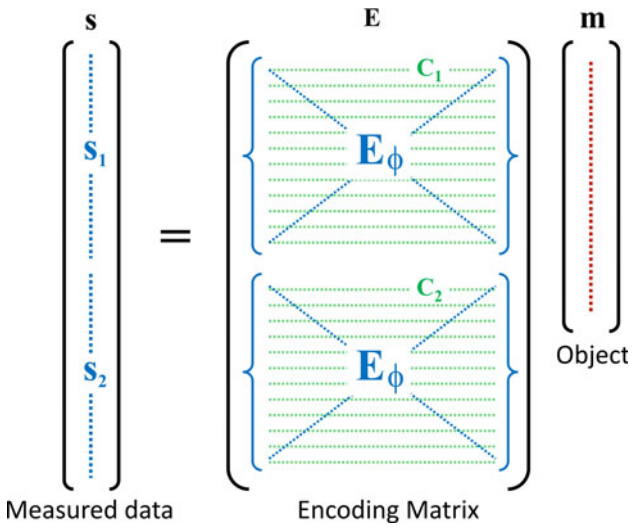

Fig. 4 Cartoon representation of Eq. 5, here assuming just two RF coils ($N_c = 2$) for simplicity, to demonstrate how the full encoding matrix $\mathbf{E}$ is composed of N_c repeats of the sub-matrix $\mathbf{E}_\phi$, where each repeat is modulated by the RF coil sensitivities $\mathbf{C}_i$. The sub-matrix $\mathbf{E}_\phi$ has unit magnitude throughout, but contains the phase information due to the encoding from the SEMs—as well as, optionally, the off-resonance due to B_0 inhomogeneities

requirement by a factor N_c, but at the expense of increased computation time for each CG iteration, as the application of the full encoding matrix needs to be calculated in N_c subsets.

It is also possible to make more dramatic reductions in the memory requirements if compromises can be made with respect to the quality of the reconstruction. Equation (5) can be rewritten:

$$\mathbf{s}^{\mathbf{F1}} = \mathbf{E}^{\mathbf{F1}}\mathbf{m}, \tag{6}$$

where the superscript F1 denotes a 1D Fourier transform along the readout direction. The 4D-RIO trajectory is quite different from conventional encoding methods, but it is still composed of the concatenation of multiple readout periods during which the encoding field is constant. Taking a Fourier transform along each of these periods, therefore, projects the data onto the contours of each encoding field, including the effects of the prephasing. Each column of $\mathbf{E}^{\mathbf{F1}}$ therefore has the bulk of its energy focused at a single frequency for each readout period, meaning that it can be well approximated by a sparse matrix. The simplest approach to make a sparse representation of $\mathbf{E}^{\mathbf{F1}}$ is to keep only entries above a given amplitude threshold.

For the 4D-RIO trajectory, Eq. (5) can also be rewritten:

$$\mathbf{s}^{\mathbf{F2}} = \mathbf{E}^{\mathbf{F2}}\mathbf{m}, \tag{7}$$

where the superscript F2 denotes a 2D Fourier transform along the readout direction and along the spokes direction. A physical intuition for this space is more difficult to conceptualize, but it turns out that $\mathbf{E}^{\mathbf{F2}}$ can also be well approximated by a sparse matrix. We therefore decided to compare the quality of the reconstructions obtained when using sparse representations of $\mathbf{E}^{\mathbf{F1}}$ or $\mathbf{E}^{\mathbf{F2}}$ with different proportions of the matrices set to zero.

Materials and methods

Simulating the effects of prephasing

To test the effect of adding prephasing to the CRCPO trajectory, or that of removing prephasing from the 4D-RIO trajectory, data were simulated for a digital phantom at 256 × 256 resolution for each trajectory. Eight RF coil maps were derived using the Biot-Savart Law for a single coil of wire. Gaussian distributed noise was added at the 5 % level. Reconstruction was identical to experimental data, except that 25 CG iterations were performed for all simulated data.

4D-RIO experiments

All experiments were performed with the same custom hardware setup as described in [1]. This consists of a custom-built insert coil capable of generating fields which closely approximate the quadrupolar mathematical functions $x^2 - y^2$ and $2xy$ (but with both fields rotated by 22.5° with respect to the conventional x and y axes of the magnet) [10], driven by high performance amplifiers of the same specification as the linear gradient amplifiers on the 3T clinical imaging system (MAGNETOM Trio Tim, Siemens Healthcare, Erlangen, Germany). Using a modified version of an architecture designed for parallel RF excitation [11], we were able to develop pulse sequences with simultaneous waveforms on the linear and quadrupolar SEM channels. An integrated RF head coil (Siemens), with single-channel transmit and 8-channel receive, was fitted inside the insert-gradient coil.

A 190 mm diameter cylinder containing many Plexiglas tubes (to provide structure) was used for the phantom measurements, filled with water doped with nickel sulfate and sodium chloride. All measurements were performed at isocenter, using the linear z-gradient for slice-selection with a slice thickness of 5 mm. Maps of the RF sensitivities and SEM fields are required for image reconstruction. These were obtained from a 300 × 300 matrix GRE acquisition, 220 mm FoV with 8 echoes (echo spacing 4 ms). For the RF sensitivity maps it was sufficient to use data from only the first echo, estimating the sensitivity maps using the adaptive method described in [12], followed by smooth surface fitting to allow extrapolation beyond the regions of low signal intensity. To map the quadratic SEMs, the 8 echoes were repeated with small

blips on one of the quadratic SEM channels between each echo, which, after removing the phase from the scan without blips, could be used to directly measure the SEM magnitude.

It should be noted that the SEM mapping procedure differs slightly from that described in [1], where the B_0 contribution was calculated from early echoes without blips and removed from later echoes including blips. It was since discovered that this method was introducing a bias in the SEM estimation. We found that the same subtraction of the phase (late echoes minus early echoes) results in a small residual field, linearly varying in the readout direction, even when no blips are applied. This is most likely due to small timing errors or eddy currents from the imaging gradients themselves. This small but reproducible offset, however, was sufficient to affect the reconstruction of 4D-RIO data—and was found to be the principal source of the error which meant that further calibration of the SEMs was necessary in earlier experiments [1]. For the reconstructions presented here, no further modification of the SEMs was required following their measurement.

For the SEM mapping, the maps obtained from the phantom were also used for reconstructing the in vivo data, as the phantom provides better and more consistent coverage. For the RF maps the data were taken from the same session as the 4D-RIO acquisition, as RF sensitivity maps are expected to vary somewhat depending on the object under investigation. B_0 maps were obtained from the same multi-echo GRE scan, and these were also included in the 4D-RIO reconstruction.

The 4D-RIO data were all acquired with a split readout GRE (as described in [1]) with two 2.56 ms duration readout blocks starting at 3.52 and 8.92 ms following the center of the excitation RF pulse (flip angle 15°, slice thickness 5 mm) and a TR of 100 ms. The nominal FoV was set to 252 mm, such that if the two linear components or the two quadratic components of the trajectory were to be played independently, they would correspond to a 'square' (i.e. 256 readout points along 256 spokes) projection-reconstruction acquisition at this FoV.

Safety considerations

Previous results presented using the 4D-RIO trajectory have all been phantom studies, and this work represents the first demonstration of the method in vivo—a single healthy human subject was scanned following IRB approval. When testing new methodologies that utilize custom hardware, it is particularly important to consider safety implications which may arise. The safety-relevant construction features and practical assessment of the safety of the PatLoc insert for human scanning have been reported previously [13]. The principal additional risk factor when running the 4D-RIO trajectory compared to conventional trajectories using only the linear gradients is the potential for PNS caused by induced voltages in the body as a result of switching the currents in the SEM generating coils. Although the expected reduced risk of PNS was one of the original motivations for investigating nonlinear encoding fields, the models we have available for predicting PNS are only empirical, and PNS thresholds are known to vary considerably between subjects [14], so we chose a cautious approach for this study. Using simulated fields for the linear and nonlinear SEMs, including concomitant components, we evaluated the 'worst-case' addition of all SEMs during switching of the fields. We then introduced a global scale factor for the amplitude of current for all SEM pulses, and started all measurements with the scale reduced sufficiently for the 'worst-case' field change to be within a conservative threshold of 20 T/s. The scale factor could then be raised slowly in increments of 10 % to reach the desired switching rate (as the difference between perception of PNS and painful PNS can be as small as 15 % [15]), checking with the subject between each run that no PNS was experienced. For the sequences used here, the starting scale factor was 0.4, requiring 10 steps to reach full switching rate.

Image reconstruction

All 4D-RIO data reconstruction was performed in MATLAB (The Mathworks, Natick, MA), running 64-bit Linux either on a desktop PC (2.66 GHz Intel Core 2 Duo processor, 4 GB RAM) or on a compute server (2.26 GHz Intel Xeon 7500-series, 1 TB RAM). 20 CG iterations were applied to estimate $\mathbf{m}$ in Eqs. (5–7). To test the quality of the image reconstruction with different storage requirements, the sub-matrix of the encoding matrix ($\mathbf{E}_{\phi}^{\mathbf{F1}}$ or $\mathbf{E}_{\phi}^{\mathbf{F2}}$) for the $128 \times 128 \times 8$ data was stored in full and then thresholded at a range of percentiles of the magnitude values, corresponding to keeping 1, 2, 5, 10 and 20 % of the matrix entries.

After observing that the principal artifact associated with reconstructions using sparse versions of $\mathbf{E}_{\phi}^{\mathbf{F1}}$ appeared to originate from the center of the FoV, we also tested a third variation of the sparsification: the same thresholding of the magnitude values, but with all columns of $\mathbf{E}_{\phi}^{\mathbf{F1}}$ corresponding to voxels within a circular mask at the center of the FoV preserved entirely. We chose a circle radius of 5 % of the FoV, corresponding to an increase in the number of non-zero entries in the sparse version of $\mathbf{E}_{\phi}^{\mathbf{F1}}$ of 0.81 % compared to the total entries in the matrix.

Results

Simulating the effects of prephasing

Figure 5 shows the reconstructed images using the CRCPO and 4D-RIO trajectories, with and without prephasing. As expected from the local *k*-space plots in Fig. 2, the CRCPO trajectory (Fig. 5a) exhibits poor resolvability of image features, especially in the azimuthal direction. The addition of prephasing (Fig. 5b) gives a high quality reconstruction. For 4D-RIO (Fig. 5d) there is evidence of a slight loss of resolution towards the center—again consistent with the local *k*-space plots. For 4D-RIO with prephasing removed (Fig. 5c) the reconstruction is of poor quality across most of the object.

4D-RIO experiments

No PNS or other unusual sensation was reported by the subject during or after the scan. The high-resolution reconstructions of 4D-RIO data collected on the phantom and in the brain of a human volunteer are shown in Fig. 6. In the phantom image there is no significant image artifact within the object, but a small amount of superfluous signal apparent outside of the object (bottom right of Fig. 6a) in the region where the RF maps needed to be extrapolated from the measured data. In the human data there is evidence of minor ringing effect towards the center of the FoV. As this artifact is not present in the phantom data, it is most likely attributable to subject motion.

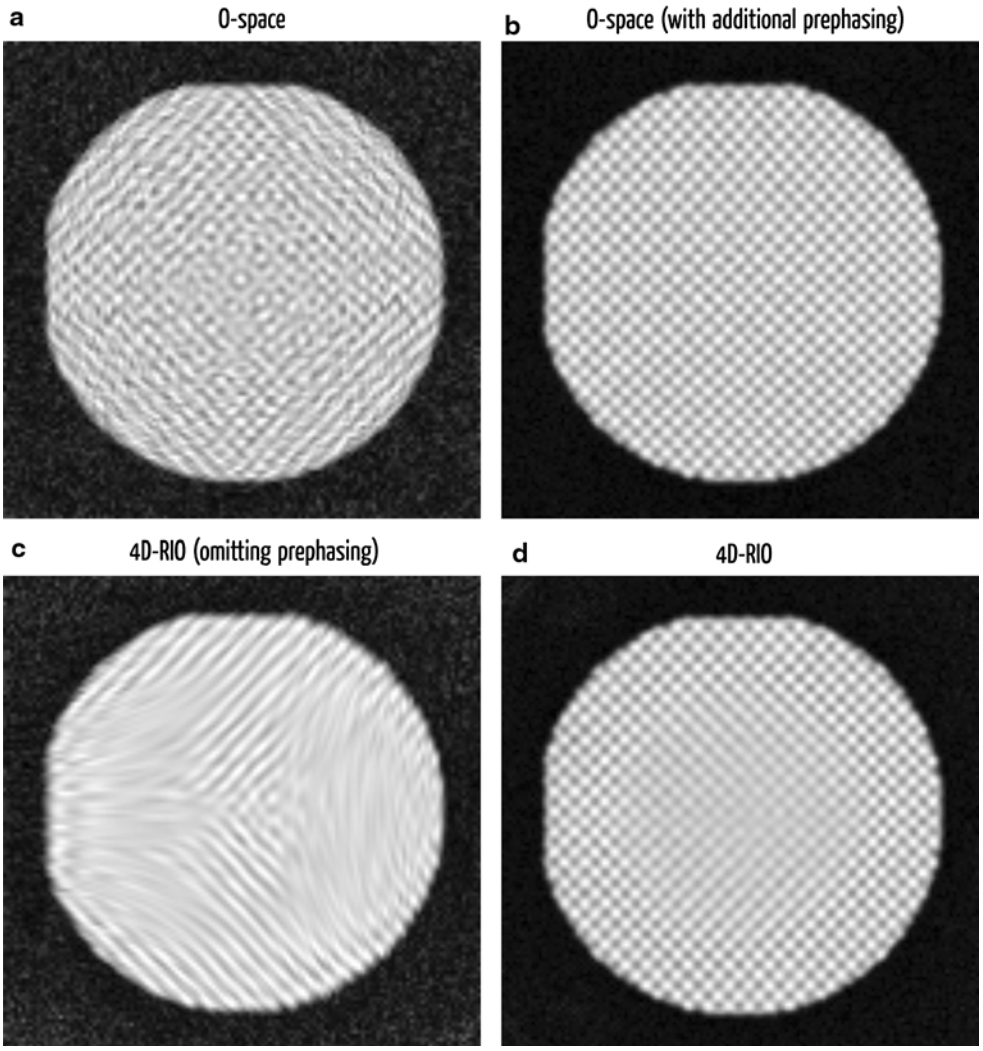

Fig. 5 Reconstructions of simulated data using the same trajectories as shown in Figs. 2 and 3. Data were simulated at 64 × 64 samples (64 × 65 for O-space) and reconstructed to a 128 × 128 grid using 25 CG iterations. The differences in local resolution can be explained by comparing the local *k*-space plots from Fig. 2

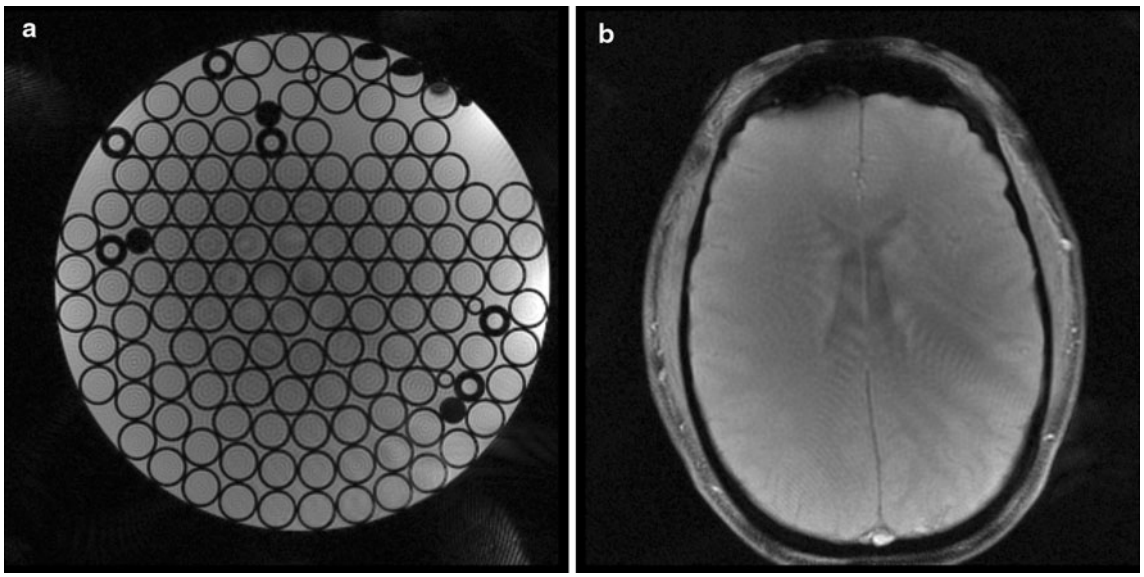

Fig. 6 Reconstructions of experimental 4D-RIO data collected at 256 × 256 resolution, 8 RF coils, onto a grid 320 × 320 using **a** a doped water phantom and **b** a healthy volunteer

The raw data from 4 of the 8 RF channels from the phantom scan are shown in Fig. 7, along with images following a 1D Fourier transform only along the readout direction, or a 2D Fourier transform along both the readout direction and the spokes direction. After the 1D Fourier transform we expect to see a set of projections along each of the encoding fields applied during each readout spoke. After the second Fourier transform, a physical interpretation of the space we are observing is more difficult to derive. It is interesting to note, however, that structural features of the object being imaged are clearly identifiable in all three spaces. The image of the data after a 2D Fourier transform even closely resembles the object itself, despite the second transform being along the direction of the rotating spokes. Careful examination of these images also reveals that in this space partial aliasing of the signal occurs (e.g. compare the features visible in channel 1 vs. channel 2).

Figure 8 shows the reconstructed images obtained with various degrees of sparsification of $\mathbf{E}_{\phi}^{\mathbf{F1}}$ or $\mathbf{E}_{\phi}^{\mathbf{F2}}$. For the case of $\mathbf{E}_{\phi}^{\mathbf{F1}}$ the quality of the reconstruction appears to be good towards the edge of the FoV using even as little as 2 % of the full matrix, whereas noise dominates at 1 %. Even using 20 % of the matrix, however, there is a noticeable ringing-like artifact which appears to originate at the center of the FoV, and this artifact becomes more prominent as the level of sparsity is increased.

For the case of $\mathbf{E}_{\phi}^{\mathbf{F2}}$ the degradation of the image quality is more even across the FoV—but the images at 10 and 5 % are noticeably 'noisier' (where the 'noise' has been introduced by the reconstruction rather than the acquisition) than for $\mathbf{E}_{\phi}^{\mathbf{F1}}$. At 2 % sparsification, and more clearly at 1 % sparsification, there are three regions where the image quality is more severely degraded. These regions are towards the edge of the FoV, and rotated by 120° with respect to each other. Interestingly, this same threefold rotation symmetry is observable in the local *k*-space plots for 4D-RIO (most clearly in Fig. 2c, but also visible in Fig. 2d when looking at the orientation of the 'poles' of the local *k*-space pattern).

As demonstrated in the right-most column of Fig. 8, the inclusion of the extra columns of $\mathbf{E}_{\phi}^{\mathbf{F1}}$, which correspond to voxels within the central mask, is sufficient to dramatically reduce the ringing artifact visible in the left-most column. Whereas at 5% sparsity the thresholded $\mathbf{E}_{\phi}^{\mathbf{F1}}$ matrix leads to very strong ringing from the center outwards across a large section of the FoV, the inclusion of the center mask leaves the artifact barely discernible, even across regions far larger than the extent of the mask.

Table 1 shows the memory requirements and reconstruction times for various reconstruction pipelines. Reconstruction times are given for running on the compute server and, where possible, on the desktop PC. It should be noted that although the desktop PC we were using has 4 GB of RAM, including overhead for Matlab itself, as well as other variables, storing a matrix as large as 3.36 GB is not practicable. The largest matrix we found that could be handled easily was approximately 1.5 GB, with a more than tenfold increase in reconstruction time when this was extended to 2.0 GB. On the compute server with 1 TB RAM, the reconstruction times all scaled, as expected, with a linear dependence on matrix size. Also included in

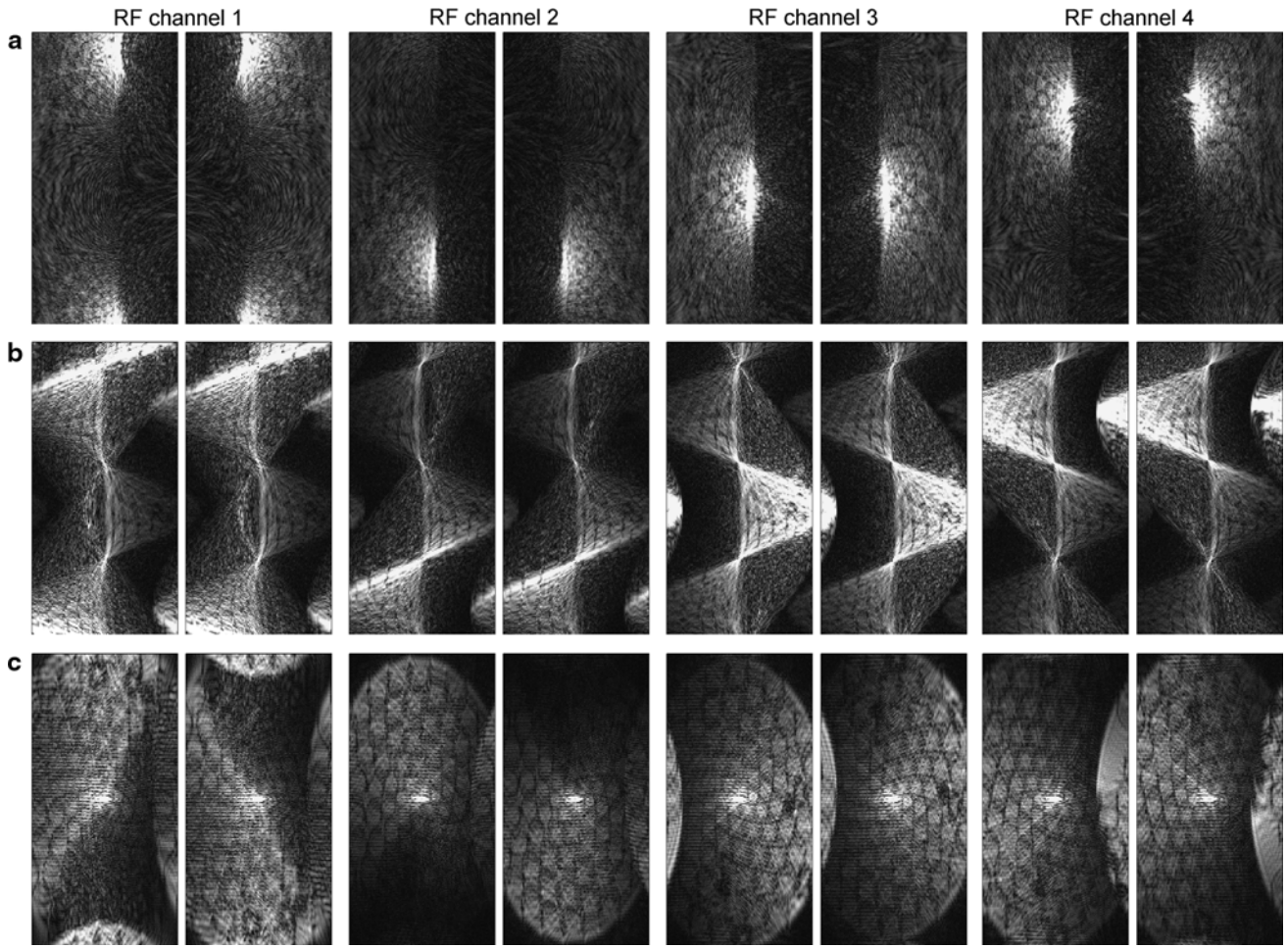

Fig. 7 **a** Magnitude of 4D-RIO raw data on 4 of the 8 RF channels (the same data as shown in Fig. 6a). The readout direction runs from left to right, with a gap at the point where the pulse sequence splits for the sweep-back of the linear encoding. The spokes direction runs from *bottom* to *top*. **b** The same data after a Fourier transform in the readout direction. **c** The same data after a 2D Fourier transform in both the readout direction and the spokes direction

Table 1 are the storage requirements—it should be noted that creating a sparse matrix with 20 % of the entries of the full matrix does not save 80 % of the memory. The additional information required to describe where in the matrix the nonzero elements are located also requires memory, explaining why storing 1–20 % of the full 3.36 GB matrix required between 0.10 and 2.0 GB.

Discussion

The simulations demonstrated the large improvement that prephasing can have on the quality of reconstructed images acquired using the CRCPO trajectory, as well as the degradation of image quality in the 4D-RIO trajectory if the implicit prephasing is omitted. We did not have the hardware available to experimentally confirm this result, but this remains an interesting comparison for future work.

We have successfully demonstrated that high resolution images can be obtained using the 4D-RIO trajectory, and in the first subject scanned there was no evidence of PNS. In the future it may be useful to conduct a more complete stimulation study (as performed in [15] and [16],) for the nonlinear SEMs, especially as new coils are built capable of faster switching rates.

Although it may appear from Fig. 5 that CRCPO with prephasing (Fig. 5b) is superior to 4D-RIO with prephasing (Fig. 5d) due to the blurring evident towards the center of the FoV, this is a consequence of the smaller local *k*-space coverage in the center (c.f. Fig. 2b, d) of the particular 4D-RIO trajectory used, and of the difficulty of matching it fairly to CRCPO. If desired, the 4D-RIO trajectory could be designed with a stronger linear component, thereby also increasing the local *k*-space coverage at the FoV center.

It is clear that encoding with nonlinear SEMs can lead to some imaging properties which defy what we might

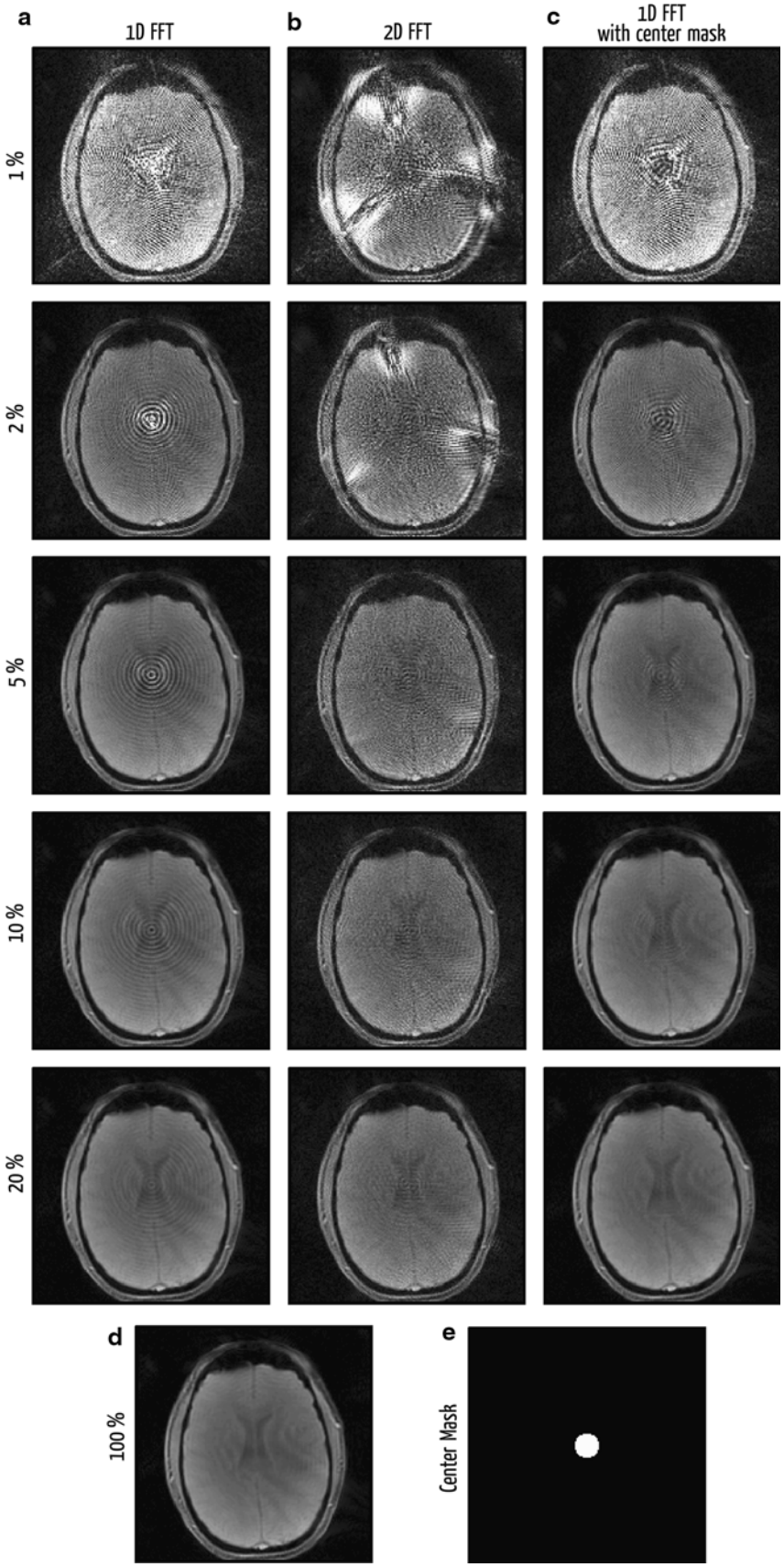

Fig. 8 Comparison of reconstructions of the same 4D-RIO data (each after 20 CG iterations) by retaining different proportions of the sub-matrix $\mathbf{E}_\phi$ of the encoding matrix. Data were first Fourier transformed either **a** 1D (along the readout direction) or **b** 2D (also along the spokes direction). **c** The same reconstructions as **a**, but always including encoding matrix values falling within the central mask shown in **e** (representing an additional 0.81 % of the matrix). **d** The reconstruction using 100 % of the encoding matrix, which is identical when using the original encoding matrix or Fourier transformed versions

Table 1 Memory requirements and reconstruction times for a range of reconstruction pipelines

Data samples	Recon grid size	Stored matrix	Memory to store matrix (GB)	Time to build matrix (sec)	Time for each CG iteration (sec)	Total recon time (min)
256^2	320^2	$\mathbf{E}$	429	990	120	57
128^2	160^2	$\mathbf{E}$	26.8	90	20	8
128^2	160^2	$\mathbf{E}_\phi^{F1}$ or $\mathbf{E}_\phi^{F2}$	3.36	40	45	16
128^2	160^2	1–20 % of $\mathbf{E}_\phi^{F1}$ or $\mathbf{E}_\phi^{F2}$	0.10 to 2.0	40	18–47 (18–500[a])	7–16 (7–170[a])

Reconstruction times shown are approximate

[a] Reconstruction time when running on the desktop PC rather than the compute server. Note that reconstruction times for the sparse matrices were similar between the compute server and the desktop PC for all matrix sizes except for 2.0 GB, where the desktop PC took more than tenfold longer

intuitively expect from conventional encoding with linear SEMs. We find the observation that structural features of the object under investigation can be seen in the raw data space after one Fourier transform and after two Fourier transforms (as shown in Fig. 7) to be a particularly good example of such an unusual property. This property appears to be related to the observation that linearly encoding images with quadratic prephasing can lead to a distribution of signals in k-space which resembles the object itself [6, 17]. With conventional linear encoding of a purely real object, all spins throughout the excited slice will simultaneously experience an echo at the time when the center of k-space is acquired, i.e. when $(k_x, k_y) = (0, 0)$. With nonlinear encoding fields, however, the echoes no longer necessarily occur simultaneously. As was previously demonstrated for the 4D-RIO trajectory, local echoes occur only when the saddle center of the net encoding field passes through a particular region [1]. As the center of the saddle traces out a star-pattern through consecutive readouts, so the dominant signal will have been collected in a pattern resembling polar coordinates. This explains why the raw data shown in Fig. 7a approximately resemble a representation of the object in polar coordinates, with the readout direction along the radial axis and the spokes direction along the polar angle. After a single Fourier transform along the readout direction, as shown in Fig. 7b, the signals bear some semblance to a sinogram, but with the unconventional property that object features are still recognizable; in a true sinogram all such features are blurred out in the polar direction. We have so far been unable to develop an intuitive explanation for the observation that the object is so clearly recognizable in the signals after the second Fourier transform in the spokes direction (Fig. 7c).

It is interesting to compare the difference in how the reconstructed images degrade with increasing proportions of the encoding matrix discarded, as shown in Fig. 8. When the 1D FFT reconstruction pipeline is used, and $\mathbf{E}_\phi^{F1}$ is the matrix which is thresholded, the dominant artifact introduced is the ringing-like effect extending from the FoV center. It appears that the center of the FoV deteriorates first because all readout lines contain strong signals from the center, whereas the edge of the FoV contributes strong signals to only a few of the readout spokes. As the $\mathbf{E}_\phi^{F1}$ matrix becomes thresholded to a greater degree, it seems that more conflicting signals arise in the center, manifesting as this ringing-like artifact. This also explains why the center mask is so effective at suppressing the ringing artifact: the region of $\mathbf{E}_\phi^{F1}$ corresponding to where the conflicting signals might be problematic is kept intact.

When the 2D FFT reconstruction pipeline is used, and $\mathbf{E}_\phi^{F2}$ is the matrix which is thresholded, the reconstructed image deteriorates in a less structured way, with noise-like artifacts visible throughout the image even with the threshold as high as 20%. It appears that the second Fourier transform distributes the effect of conflicting signals more evenly across the FoV, meaning that the use of a center mask would have no appreciable effect on the image reconstruction quality (we also verified this experimentally, but it is not shown here in the figures).

We found that by making a sparse approximation to the $\mathbf{E}_\phi^{F1}$ matrix, and then restoring the parts of the matrix corresponding to voxels within the central mask, we were able to fit the matrix into the memory of a mid-range desktop PC. This allows image reconstructions in a more reasonable time than the alternative approach of re-calculating each line of the matrix as it is required in each CG iteration. Clearly there is a penalty to pay for such an approximation, as it will introduce obvious artifacts if pushed too far. It may be the case that an approximate reconstruction is sufficient at scan time to verify the quality of the data, with a more accurate reconstruction performed afterwards off-line.

Choosing the degree to which the matrix is sparsified will depend on the number of data samples and the desired resolution of the image reconstruction, as well as the RAM available on the computer used for reconstruction. The examples given here were all reconstructed to 2D images, and it is likely that one might be willing to wait longer to get a more accurate reconstruction. However, if these generalized encoding methods are to be used for 3D image reconstruction (as might be performed with new nonlinear SEM designs such as those in [7, 18]) then the encoding matrix will be very much larger. Considerable savings in the reconstruction time will then need to be made, even if more use is made of parallel computing, either with multi-processor CPUs or general purpose graphics cards (as recently reported for a similar reconstruction problem in [19]).

Conclusion

We have successfully collected and reconstructed in vivo human head images using the 4D-RIO sequence, combining simultaneous encoding with linear and nonlinear encoding fields. We have also made use of the property that, although the Fourier transform cannot be used directly to reconstruct the data, it can still be helpful to put the encoding matrix into a space where it can be approximated by a sparse matrix. Sparsifying the encoding matrix can lead to faster reconstructions with smaller memory requirements, albeit at the expense of a loss of image quality.

Acknowledgments The authors wish to thank Andrew Dewdney of Siemens Healthcare, Erlangen, Germany for making possible the hardware integration of the custom-built insert coil, Dr Wilfried Reichardt (University Medical Center Freiburg) for medical support for in vivo measurements, as well as Kelvin Layton of the University of Melbourne for proof-reading the manuscript. This work was performed as part of the INUMAC project, supported by the German Federal Ministry of Education and Research, grant #13N9298.

References

1. Gallichan D, Cocosco CA, Dewdney A, Schultz G, Welz A, Hennig J, Zaitsev M (2011) Simultaneously driven linear and nonlinear spatial encoding fields in MRI. Magn Reson Med 65:702–714
2. Hennig J, Welz AM, Schultz G, Korvink J, Liu Z, Speck O, Zaitsev M (2008) Parallel imaging in non-bijective, curvilinear magnetic field gradients: a concept study. Magn Reson Mater Phy 21:5–14
3. Schultz G, Ullmann P, Lehr H, Welz AM, Hennig J, Zaitsev M (2010) Reconstruction of MRI data encoded with arbitrarily shaped, curvilinear, nonbijective magnetic fields. Magn Reson Med 64:1390–1403
4. Stockmann JP, Ciris PA, Galiana G, Tam L, Constable RT (2010) O-space imaging: highly efficient parallel imaging using second-order nonlinear fields as encoding gradients with no phase encoding. Magn Reson Med 64:447–456
5. Ciris PA, Stockmann JP, Tam L, Constable RT (2009) O-space imaging: tailoring encoding gradients to coil profiles for highly accelerated imaging. In: Proceedings of the 17th annual meeting, international society of magnetic resonance in medicine, Honolulu, Hawaii, USA, p 4556
6. Witschey W, Cocosco CA, Gallichan D, Schultz G, Weber H, Welz AM, Hennig J, Zaitsev M (2011) Localization by nonlinear phase preparation and K-space trajectory design. Magn Reson Med (Early View online). doi:10.1002/mrm.23146. http://onlinelibrary.wiley.com/doi/10.1002/mrm.23146/abstract
7. Littin S, Welz AM, Gallichan D, Schultz G, Cocosco CA, Hennig J, DeBoer W, Zaitsev M (2011) Planar gradient system for imaging with non-linear gradients. In: Proceedings of the 19th annual meeting, international society of magnetic resonance in medicine, Montreal, Canada, p 1837
8. Pruessmann KP, Weiger M, Börnert P, Boesiger P (2001) Advances in sensitivity encoding with arbitrary k-space trajectories. Magn Reson Med 46:638–651
9. Schultz G, Gallichan D, Reisert M, Zaitsev M, Hennig J (2011) Fast image reconstruction for generalized projection imaging. In: Proceedings of the 19th annual meeting, international society of magnetic resonance in medicine, Montreal, Canada, p 2868
10. Welz AM, Cocosco CA, Dewdney A, Schmidt H, Jia F, Korvink J, Hennig J, Zaitsev M (2009) PatLoc gradient insert coil for human imaging at 3T. In: Proceedings of the European society of magnetic resonance in medicine and biology, Antalya, Turkey, p 316
11. Fontius U, Baumgartl R, Boettcher U, Doerfler G, Hebrank F, Fischer D, Jeschke H, Kannengießer S, Kwapil G, Nerreter U, Nistler J, Pirkl G, Potthast A, Roell S, Schor S, Stoeckel B, Adelsteinson E, Adriany G, Alagappan V, Gagoski B, Setsompop K, Wald L, Schmitt F (2006) A flexible 8-channel RF transmit array system for parallel excitation. In: Proceedings of the 14th annual meeting, international society of magnetic resonance in medicine, Seattle, USA, p 127
12. Walsh DO, Gmitro AF, Marcellin MW (2000) Adaptive reconstruction of phased array MR imagery. Magn Reson Med 43:682–690
13. Cocosco CA, Dewdney AJ, Dietz P, Semmler M, Welz AM, Gallichan D, Weber H, Schultz G, Hennig J (2010) Safety considerations for a PatLoc gradient insert coil for human head imaging. In: Proceedings of the 18th annual meeting, international society of magnetic resonance in medicine, Stockholm, Sweden, p 3946
14. Schaefer DJ, Bourland JD, Nyenhuis JA (2000) Review of patient safety in time-varying gradient fields. J Magn Reson Imaging 12:20–29
15. Irnich W, Schmitt F (1995) Magnetostimulation in MRI. Magn Reson Med 33:619–623
16. Ham C, Engels J, van de Wiel G, Machielsen A (1997) Peripheral nerve stimulation during MRI: effects of high gradient amplitudes and switching rates. J Magn Reson Imaging 7:933–937
17. Wedeen VJ, Chao YS, Ackerman JL (1988) Dynamic range compression in MRI by means of a nonlinear gradient pulse. Magn Reson Med 6:287–295
18. Juchem C, Nixon TW, McIntyre S, Rothman DL, de Graaf RA (2010) Magnetic field modeling with a set of individual localized coils. J Magn Reson 204:281–289
19. Bieri MA, Barmet C, Wilm BJ, Pruessmann KP (2011) Versatile higher-order reconstruction accelerated by a graphics processing unit (GPU). In: Proceedings of the 19th annual meeting, international society of magnetic resonance in medicine, Montreal, Canada, p 2545